Neuron, Vol. 38, 529–545, May 22, 2003, Copyright ©2003 by Cell Press

New Paradigm for Optical Imaging: Temporally Encoded Maps of Intrinsic Signal

Neurotechnique

Valery A. Kalatsky and Michael P. Stryker*
W.M. Keck Foundation Center for Integrative Neuroscience
Department of Physiology
University of California, San Francisco
San Francisco, California 94143

Summary

We present a new technique for acquiring and analyzing intrinsic signal optical images of brain activity, using continuous stimulus presentation and data acquisition. The main idea is to present a temporally periodic stimulus and to analyze the component of the response at the stimulus frequency. Advantages of the new technique include the removal of heart, respiration, and vasomotor artifacts, a dramatic increase in spatial resolution, and a 30-fold or greater reduction in acquisition time. We also present a novel approach to localizing instantaneous neuronal responses using time-reversed stimuli that is widely applicable to brain imaging. To demonstrate the power of the technique, we present high-resolution retinotopic maps of five visual areas in mouse cortex and orientation maps in cat visual cortex.

Introduction

The cortex of the mammalian brain is a quasi-two-dimensional structure in which cells within each radial column share some response properties. Tangentially, the cortex is divided into many functional areas, and the cortical columns within many of the known areas are organized into maps. These maps have the property that similar stimuli or similar responses are represented by columns of cells that lie near to one another in the cortex. In sensory cortex, such functional maps do not provide complete information about stimulus preferences of a single neuron. Rather, they average the common elements of the stimulus preferences of neurons in the column.

Most methods of neural functional evaluation use randomly interleaved, episodic stimulus presentation: either the responses following the many repetitions of each particular stimulus are averaged in relation to the time of onset of the stimulus, or else (in the approach referred to as reverse correlation) the stimuli preceding the neuronal responses are averaged in relation to the time of the response. These approaches are well suited to study a passive system or a system without internal dynamics. They assume that the noise is random and will average out over many trials. If, however, the system has dynamics, then the noise will not be random, and the averaging procedure will irreversibly mix the signal with the noise.

Optical imaging has proven to be a successful technique for observing neural activity over large cortical areas (Blasdel and Salama, 1986; Grinvald et al., 1986). Conventional methods for data acquisition and analysis of the intrinsic signal optical responses are based on episodic presentation of stimuli where the transient responses to the different stimuli are averaged and normalized by that to a "blank" stimulus to produce the cortical map (Bonhoeffer and Grinvald, 1996). In this paper, we present another general paradigm for stimulus presentation and analysis of optical imaging data: continuous-periodic stimulation combined with continuous data acquisition. Continuous stimulation offers the advantage of exhaustive coverage of stimulus space, so that every neuron is exposed to its optimal value of the stimulus parameter that is varied continuously. Periodic stimulation offers the supreme advantage of effective separation of the stimulus-evoked responses from intrinsic noise using Fourier analysis of the continuous data stream, as was shown previously for assessment of topography (Engel et al., 1994, 1997; Sereno et al., 1995; DeYoe et al., 1996) and other features of brain activity (Boynton et al., 1996) by functional magnetic resonance imaging in human visual cortex. We demonstrate the generality and power of this paradigm using intrinsic signal optical imaging to make maps of orientation columns and topography. We also demonstrate a new procedure by which instantaneous neuronal responses may be calculated from the slow hemodynamic responses that give rise to intrinsic optical signals. Finally, we demonstrate the efficiency of the new method by comparing cortical maps made using the new paradigm to those obtained in the traditional manner by averaging the responses to episodic, randomly interleaved stimulus presentations.

The separation of neuronal responses from artifact in software, through the Fourier analysis of responses to periodic stimulation, permits a great simplification of the imaging system: it consists of a CCD camera and stimulation, acquisition, and analysis computers and requires no specialized hardware for synchronization with sources of artifact (Bonhoeffer and Grinvald 1996; Shoham et al., 1999). The simplicity of the system makes it very attractive for the neurophysiological imaging community.

Here, we develop analytical principles of the technique, describe design of the imaging system, and present our results on imaging the mouse visual cortex and rapid acquisition of orientation maps of the cat primary visual cortex.

Results

Hemodynamics and Stimulus Pattern

A major goal of systems neuroscience is to characterize the brain response to its inputs. This goal is generally pursued using a standard input-output approach, i.e., one presents input (stimulation), and after a certain delay measures output (a spike, change in membrane potential, change of light reflectance, and so on). This ap-

*Correspondence: stryker@phy.ucsf.edu

proach works well for passive systems, i.e., systems without internal dynamics. However, it can be ineffective for active systems such as the brain. An active system may produce output without external input, depending on the system's internal state. When input is actually present, the response to the input can be mixed with the ongoing activity, thus making the output noisy. Analyzing responses to episodic or randomized stimulus presentation suffers from this problem. The only way to cope with the contamination of responses by ongoing activity is to repeat presentation over and over again, hoping that it is not correlated with the ongoing activity, and average the responses. We have used periodic stimulation at a frequency selected as described below to remedy this problem.

A response of a generic nonlinear system to a periodic input can be quite complex since multiple harmonics may emerge. But the fundamental harmonic or response at the frequency of stimulation usually has greatest amplitude. Thus, by choosing the frequency of stimulation far from the system's internal oscillation frequencies, one can induce a periodic response that can be straightforwardly filtered from the noisy output by, for example, Fourier decomposition.

Intrinsic signal optical imaging of cortical activity suffers from such complex internal dynamics (Mitra et al., 1999). This technique measures changes in cortical light reflectance following local neural activation (Grinvald et al., 1986). The main contribution to the optical signal is believed to be due to the metabolically induced changes in the microcirculation (Frostig et al., 1990) and, thus, inherits all cardiovascular artifacts. The major components of the hemodynamics in this case include (cat data; arranged in descending frequency) heart beat (2–5 Hz), respiration rate (0.3–1 Hz), vasomotor signal (0.05–0.1 Hz) (Mayhew et al., 1996), and slow variation of the baseline due to the state of a subject, anesthesia, and so on (nonperiodic, characteristic time scale is 1 min and up) (Figure 1). Choosing a frequency of stimulation at one of the internal frequencies would be unwise because the response at this frequency would be dominated by the artifact and not by the induced response. The experimenter, however, can choose the stimulation frequency to be in the range 0.3–0.1 Hz or below 0.05 Hz and stay safely away from the artifacts. We actually use the former range to map retinotopy and the latter to obtain the orientation maps of the cat primary visual cortex.

The optimal stimulation frequency depends not only on the spectral window clear of the artifacts but also on the time course of the evoked intrinsic signal. Although the exact parameters of the temporal profile of the evoked intrinsic signal are species dependent, the general features are universal: the signal is biphasic and the initial phase is the fall of reflectance, the so-called "initial dip" (Frostig et al., 1990; Malonek and Grinvald, 1996), which is followed by slower increase of light reflectance (see Figure 1D). Stimulation with a period of 7–10 s equalizes the strength and duration of the down and up phases. Thus, periodic stimulation with frequency of 0.1 Hz or less is optimal in the sense that the spectral energy of the evoked signal is maximized. Higher frequencies of stimulation would not let the signal reach its peak value and would lead to shallow oscillations, and lower frequencies would dissipate energy into higher harmonics of the stimulus frequency. The fine-tuning of the optimal frequency should take into account the biological artifacts and usually is reached empirically. It should be noted that this approach makes no assumptions about the source, latency, or waveform of the signal to be analyzed. It would work equally well with arbitrary waveforms.

Conventional methods for data acquisition and analysis of the intrinsic and extrinsic optical responses are based on episodic presentation of stimuli (Blasdel and Salama, 1986; Shoham et al., 1999; Bosking et al., 2000; Issa et al., 2000; Schuett et al., 2002). That is, for construction of the orientation map in V1, one collects images while presenting a moving square- or sine-wave grating of one orientation followed by a blank screen or static image for relaxation of the response, after which the sequence is repeated for another randomly chosen orientation. The resulting transient responses to each stimulus are averaged, and the images are normalized by the response to a "blank" stimulus (or to the average "cocktail blank" response to the entire stimulus set) to produce the map of the cortical response to a given orientation. This approach irreversibly mixes the evoked responses with the signals of ongoing activity and has other major drawbacks. First, it assumes that there exists a stable baseline image that can be used as a reference for the evoked responses. This assumption is flawed since the baseline undergoes strong fluctuation of ubiquitous *1/f* character, where the power of the noise is inversely proportional to the frequency at which it is measured (see Figure 1). Second, interlacing blocks of stimulation with relaxation blocks of a static or blank screen of similar duration lengthens imaging time by a factor of two. The first shortcoming is relieved by the use of the periodic paradigm, which relies on the differential, rather than absolute, change of the signal. Imaging time is reduced by continuous stimulation, that is, the stimulus presentation traverses the stimulus parameter space in a continuous manner, which has additional benefits described below. Figure 2 demonstrates design of the stimuli for retinotopy and orientation mapping.

Designing stimuli that are both periodic and continuous may seem to be a problem at the first glance since there are very few truly cyclic stimulus spaces, like direction and orientation. Our solution is to impose periodicity by connecting the initial and final points of the stimulus parameter range, and thus to introduce one discontinuity in the cases of noncyclic stimulus space. In our experience, distinguishing responses to the stimuli adjacent to the discontinuity does not present a dilemma since they are usually well segregated spatially on the cortical surface. What may present a difficulty, however, is to account for the hemodynamic delay ϕ_d. We address this issue in the section on the experimental results below.

Imaging System

The key concern in the design of the imaging system was to meet requirements of the continuous-periodic stimulation and continuous image acquisition. Thus, the ability to transfer images from the digital camera to the host PC memory continuously in real time is required. The next consideration is to maximize the data rate

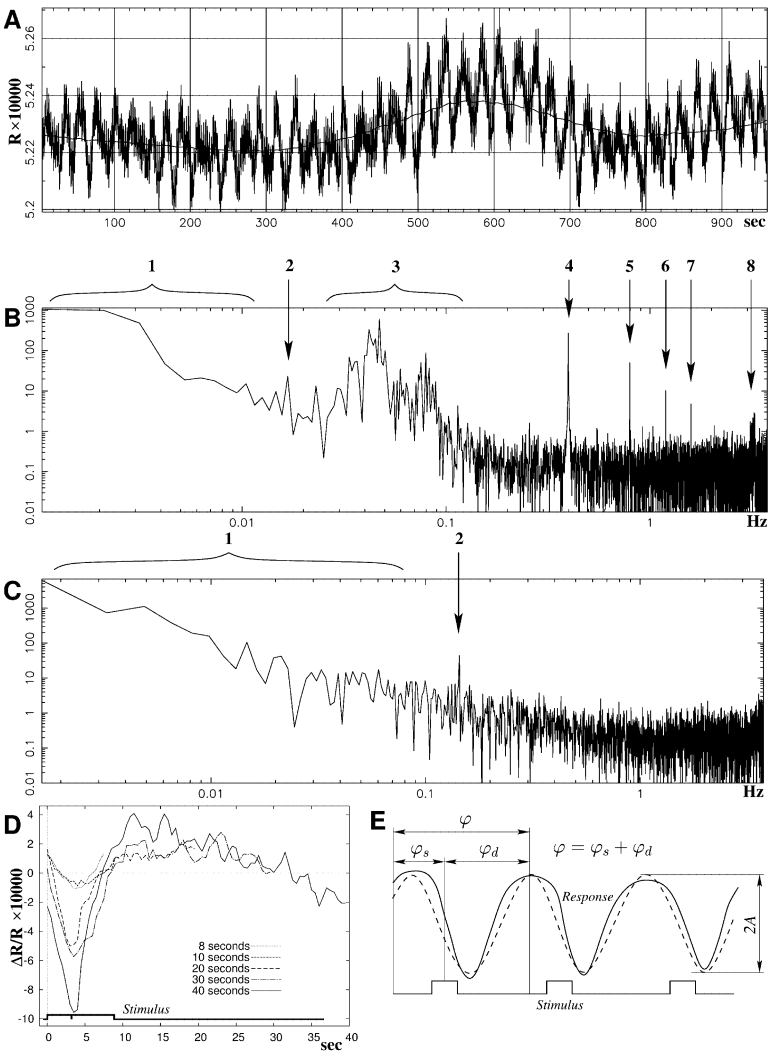

Figure 1. Time Course and Power Spectrum of the Cortical Light Reflectance

(A) Time course of light reflectance at a single pixel from a set of 7160 images of the cat primary visual cortex. The response is dominated by the vasomotor oscillations and slow variation of the baseline. To remove the slow variation, the response is time averaged over a window of integer number of stimulus cycles (2 cycles here), and the resulting curve (the smooth line) is subtracted from the response.

(B) The power spectrum of the reflectance signal plotted in (A). Components of the time series are indicated: (1) slow variation, (2) response at the frequency of stimulation (1 min period), the amplitude and phase of which are used to construct cortical maps, (3) vasomotor signal, (4) ventilation artifact (fundamental frequency), (5), (6), and (7) second, third, and fourth harmonics of the ventilation artifact, and (8) heart beat artifact. The subject was artificially ventilated; as a result, the ventilation component is strongly periodic and sharp. The high-frequency part of the spectrum (above 0.2 Hz) shows presence of the so-called shot noise due to the Poisson distributed statistics of photon counting. The mapping signal (2) is small in this case, about 3 times the noise at that frequency, interpolated from neighboring frequencies.

(C) The power spectrum of light reflectance signal at a single pixel from a set of 4593 images of the mouse primary visual cortex. Mice usually do not have vasomotor oscillations, and their heart and respiration rates are much higher than those of the cat, so that these three major sources of contamination of the evoked response are not present. The sharp spike at 0.125 Hz is the response due to visual stimulation (8 s period), which in this case is about 10 times the noise at that frequency.

(D) The hemodynamic response (fractional change of reflectance) recorded in mouse primary visual cortex (cortical area of 280 μm^2, center of the receptive field located 25° from the vertical meridian on the horizontal meridian) evoked by presentation of visual stimuli at different periods. The stimulus is a bright 1° vertical bar drifting at constant speed (77° in 9 s, see Figures 2B and 2C for stimulus design). The notch on the stimulus bar indicates the time (3 s after the bar first appears on the left side of the screen) at which the bar is over the center of the RF. 18,000 frames (10 min of recording) were temporally averaged to obtain the plots illustrated (each of which shows the response to a full stimulus cycle, which ranged from 8 to 40 s). The number of cycles averaged per trace varied according to the duration of the cycle. The response has a sinusoidal character for periods shorter than 10 s.

(E) Schematic response induced by optimal periodic stimulation. Solid curve shows response; dashed sinusoidal curve represents the Fourier component at the frequency of stimulation. The amplitude of this component *A*, normalized by the zero frequency component, is regarded as the magnitude of the evoked response, and the phase ϕ defines when the response reached its maximum relative to a reference point (e.g., beginning of the stimulus cycle). The phase or time of the response lags the time of stimulation ϕ_s by hemodynamic delay ϕ_d.

delivered by the camera while keeping complexity and cost of the system at a reasonable level. Utilization of the total data rate can be biased toward high-temporal/low-spatial or high-spatial/low-temporal resolution. Visualization of fast processes (calcium- or voltage-sensitive dye imaging) requires the former solution; we favored the latter, since intrinsic signal has slow dynamics (at least 10 times slower than the underlying neuronal activity), and hence the ultra-high speeds are not necessary. Finally, in common with requirements for conventional imaging methods, the camera's light sensor and electronics should meet certain criteria: high well capacity (the number of electrons that each photosensitive pixel can accommodate), high bit rate of digitization (the number of bits the camera's analog-to-digital board uses to convert the number of captured electrons to the final read-out value), and linearity. High well capacity is necessary to reduce the shot noise (see Figure 1B), and high bit rate preserves the small changes of light reflectance due to neuronal activity on the top of high level of reflected light (i.e., to detect low contrasts). The camera should also have frame transfer electronics to permit stable exposure durations and continuous image integration.

We have built two systems meeting all these requirements. The first one is based on Princeton Instruments Pentamax-576 camera (5 MHz pixel rate, 384 × 288 resolution, 39 fps maximum frame rate at full resolution,

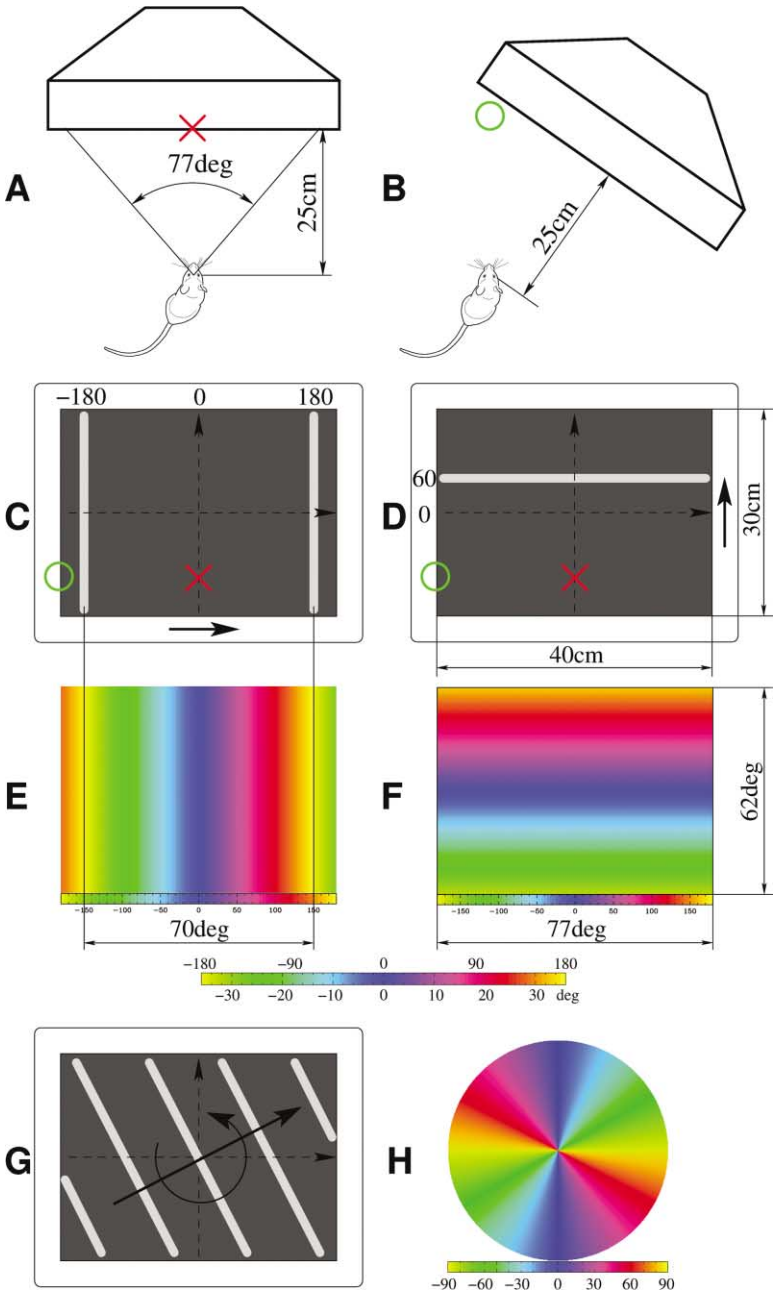

Figure 2. Stimulus Design

(A–F) Illustration of the stimuli employed to assess retinotopy of the mouse visual cortex. (A and B) Location of the monitor relative to the subject. (A) Setup used to stimulate both ipsilateral and contralateral eyes. (B) Setup used for stimulation of a wide area of the visual field of one eye, usually the eye contralateral to the hemisphere imaged. The monitor was slightly tilted forward to reduce vertical distortions due to the flat screen.

(C and D) The stimulus patterns. The stimuli are low duty-cycle square-wave gratings of low spatial frequency (0.01–0.02 cycles/degree) moving at a rate of 0.1–0.2 cycles/second. The brighter stripe has size of 1°–4°. The vertical stripes are used to stimulate the lines of constant azimuth (C) and the horizontal to stimulate the lines of constant elevation (D). Therefore, a whole line of constant azimuth or elevation is stimulated at each moment. Different lines are stimulated at different phases of the stimulus cycle. The numbers at the top (C) and on the left (D) of the monitor are the phases, measured in degrees, of the grating relative to the center of the screen. The red cross and green circle are the fixation points shown in (A) and (B), respectively.

(E and F) The color-coding used to visualize the cortical responses evoked by stimuli shown in (C) and (D), respectively. The responses evoked by the transitory configuration shown in (C) would be coded as yellow, and the ones evoked by the (D) configuration would be coded as magenta. The color-coding gradient is reversed for the stimuli drifting in the opposite direction. The color wedge shows translation of the phase of the stimulus cycle (−180° to 180°, above) to the degrees of the visual angle relative to the center of the monitor screen (−35° to 35°, below). To compensate for the flatness of the monitor, we have introduced an extra factor of 0.902 to the translation. Thus compensated, the error of the translation was not more than 1.2°.

(G and H) Illustration of the stimulus employed to assess direction and orientation selectivity of the cat visual cortex.

(G) The stimulus is a drifting and rotating square-wave grating (spatial frequency 0.1–0.4 cycles per degree); thus, it has two degrees of freedom. The drift is the fast degree of freedom (temporal frequency 1–4 cycles per second) and the rotation is the slow degree of freedom (angle speed f_r = 0.5–2 rotations per minute). The stimulus appears to be drifting only for an observer looking at the stimulus for a short period of time (a few drifting cycles). A longer integration reveals the rotation. An important advantage of this stimulus versus a rotating star of radial stripes or radial sectors is its high uniformity of the stripe velocity as function of the location on the screen, which makes it suitable for studying not only orientation selectivity but also direction selectivity. The response at $2f_r$ yields orientation selectivity; meanwhile, sum of the responses at both f_r and $2f_r$ gives directional selectivity.

(H) Color code for the orientation selectivity. Vertical orientation of the stripes is coded as blue, orientation 30° counterclockwise from that is coded as magenta, and so forth.

up to 286 fps with on-chip binning, 12-bit digitization, 400ke$^-$ well capacity). The second is based on Dalsa 1M30 camera (40 MHz pixel rate, 1024 × 1024 resolution, 30 fps maximum frame rate at full resolution, up to 129 fps with on-chip binning, 12-bit digitization, 350ke$^-$ well capacity) and PCDig frame-grabber (Coreco Imaging, Quebec, Canada). Although the systems are oriented toward intrinsic signal imaging, capability to trade off spatial resolution for temporal resolution makes both systems suitable not only for intrinsic signal imaging but also for voltage-sensitive dye imaging. The cat maps presented in this paper were obtained by the first system, and the mouse maps by the second one.

The complete imaging system consists of the image acquisition computer and camera, a second computer that produces visual (or auditory or other sensory) stimulation, and optionally a third computer for real-time analysis and data storage (functions that could be performed

on the image acquisition computer if analysis is done offline). The first two computers are synchronized using UDP or digital i/o ports. Since artifact removal is implemented by Fourier analysis, the imaging system can be assembled from off-the-shelf components and does not have any specialized or custom hardware, which is traditionally needed for synchronization with vascular and respiratory artifacts.

Images of the cortical surface illuminated by red light are acquired through a cranial window or intact skull by a CCD camera. The images are transferred to the acquisition PC, which controls the camera's function, for preprocessing and storage. It is generally unnecessary to save the raw data stream (up to 60 MByte/s in free run mode); therefore, the images are binned spatially and/or temporally, thus reducing the data rate (to 3.75–15 MByte/s or even lower). A frame header is attached to each preprocessed image and the final frame is stored locally or preferably remotely on a fast disk. Besides general experiment information, a frame header contains information about current state of stimulus. This information is either received from the stimulation computer (slave mode) or generated by the acquisition computer and sent to the stimulation computer for execution (master mode). The continuous-periodic stimulation experiments are run in the slave mode, and the conventional episodic stimulation ones are in the master mode. The stimulus patterns are generated by the stimulation PC and displayed on a high refresh rate monitor. Analysis software is run on the analysis PC concurrently with acquisition, thus giving the experimenter immediate feedback about the experiment progress and the state of the subject. We have found that the time course of the hemodynamic response is a very useful monitoring tool in addition to EKG, EEG, and other vital signs.

Retinotopy of Mouse Visual Cortex

We used stimuli shown in Figures 2C and 2D to obtain retinotopic maps, which are presented using the color scheme shown in Figures 2E and 2F. The response at the frequency of stimulation is extracted from a complete time series of image intensities acquired at each pixel, after removal of slow changes (see Figure 1). Usefulness of this removal can be demonstrated by the next example. A model response function of $R(t) = A\cos(2\pi ft) - Bt$ (sinusoidal response contaminated by a linear slow change) has the following Fourier harmonic at frequency f: $Re = A/2$ and $Im = B/2\pi f$ for a period of time TN ($T = 1/f$), where Re and Im stand for the real and imaginary components, respectively, and N is the number of cycles of the test frequency. For reasonable values like those observed experimentally of $A = 2$, $B = 100\pi f/N$, and $N = 50$, one obtains $Re = 1$ and $Im = 1$. Hence, despite our having isolated the component of the response at the stimulus frequency using Fourier analysis, failing to remove the linear slow change component from the response would cause a huge artifactual shift in its measured phase (45° in this example) as well as a change of its strength. Occasionally, it was not possible to completely remove the effect of the global changes in reflectance, which left a constant DC bias in the phases even of unresponsive brain areas. In these cases, the DC bias evaluated from the unresponsive areas was subtracted from the entire image.

The responses to the drifting horizontal grating is shown on Figures 3C–3F. We emphasize the fact that the computation of each pixel in these images was done independently. Hence, no spatial filtering was applied to these images, and the quality of the phase and magnitude maps was not artificially enhanced. The maps clearly demonstrate the superior spatial resolution of this technique. The maps resolve not only the retinotopic organization of the two primary areas (the large central spot) but also the retinotopic structure of two small areas located laterally.

The phase maps in Figures 3C and 3D do not, however, show absolute retinal position on the monitor screen because they are shifted by the hemodynamic delay ϕ_d (see Figure 1E). These are thus maps only of relative retinotopy. The hemodynamic shift is evident from the fact that the blue region (coding for the central part of the screen) appears to be located in the lateral-caudal part of the excited area and not in the middle (see Figure 3C). Such maps of the relative retinotopy can still be very useful if one is interested in measuring differential quantities such as cortical magnification factors (Daniel and Whitteridge, 1961) or in studying relation of retinotopy to other cortical functional structures (Hubel and Wiesel, 1974; Das and Gilbert, 1997; Blasdel and Campbell, 2001).

Maps of absolute retinotopy can be computed using either of two strategies to overcome the hemodynamic delay. The first strategy is to measure the delay ϕ_d directly by restricting a test stimulus to a small region of the visual field. Since the association between the stimulus and the response is unambiguous in this case, one can obtain the delay ϕ_d simply by subtraction of the stimulation time from the response time. Knowing this delay, one can then shift the whole map by $-\phi_d$ back to its absolute position. The second strategy exploits the notion of time reversal, or, since we cannot actually reverse time, we reverse the temporal sequence of the stimulus presentation (see Figures 3A and 3B). Reversal of the stimulus will lead to the reversal of the response sequence. The delay, however, should be the same in both cases. Subtracting the response time to the reversed stimulus from the response time to the direct one will produce an absolute response map that eliminates the delay (with doubled rate of the response progression, Figure 3G). Adding the two response times will produce a map of doubled delays (Figure 3H). In practice, we treat the phase (Figures 3C and 3D) and magnitude (Figures 3E and 3F) of the response as components of a vector field (a complex field). And thus, the procedures of subtraction and addition of the phase are substituted by the computationally efficient procedures of division and multiplication of the two complex fields.

The uniformity of the delay map is a good indicator of the correctness of the second method. Two cases where the method of the stimulus reversal works well are the orientation selectivity of the cat primary visual cortex, where the responses to the counterclockwise rotating stimulus (see Figure 2G) should be subtracted from those to the clockwise rotating stimulus (this is probably the best example we can think of), and the retinotopy of the mouse visual cortex, where the responses to the stimuli shown on Figures 2C and 2D

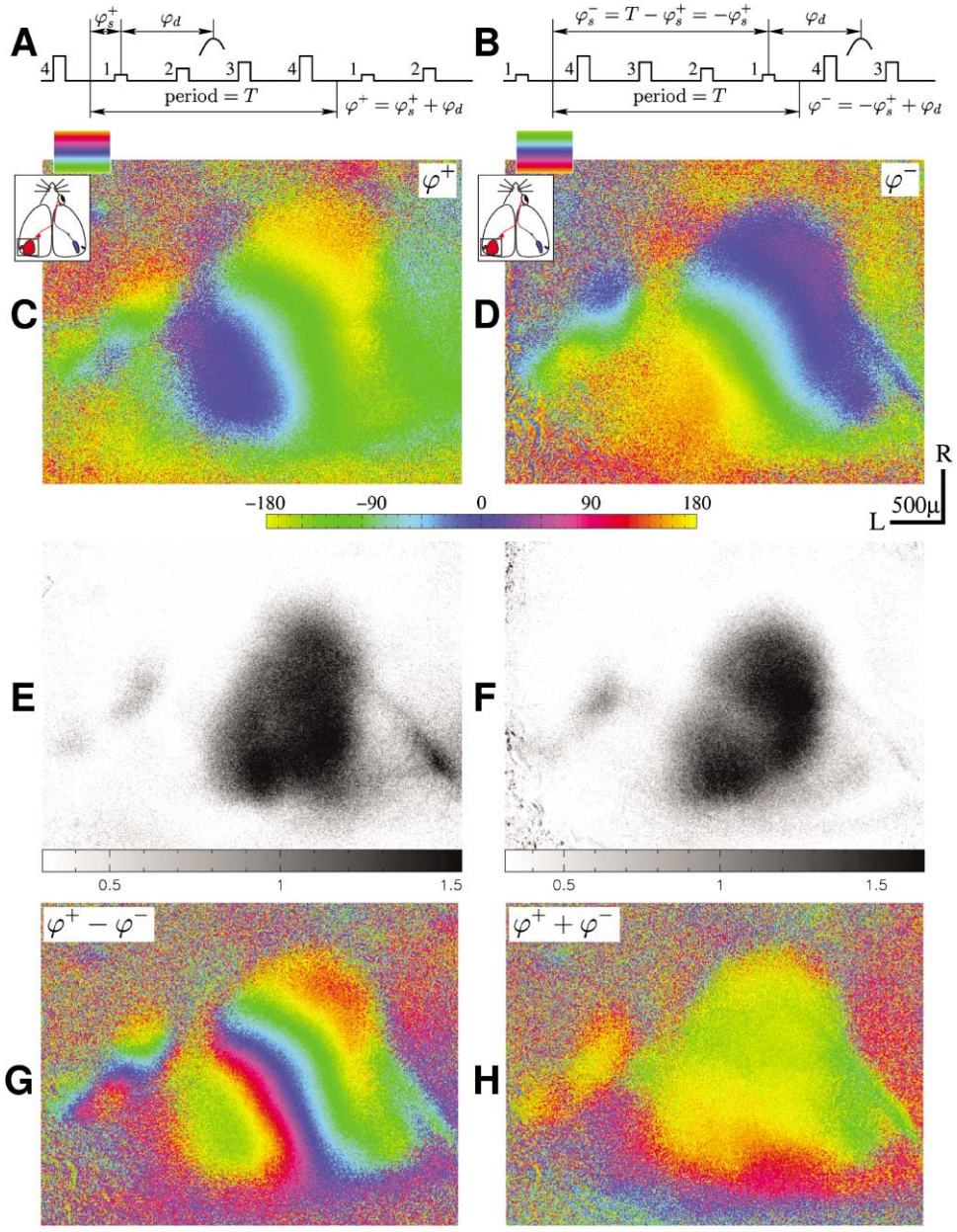

Figure 3. Maps of Relative Retinotopy and Removal of the Hemodynamic Delay

(A and B) Schematics of the hemodynamic response to the direct (A) and reversed (B) stimuli. Four pulses on the stimulus trace symbolize four different phases of the drifting square-wave grating or four different locations of the stimulating stripe (see Figure 2D). RFs at location 1 are stimulated at time ϕ_s^+ by the direct stimulus and the response peaks at time $\phi^+ = \phi_s^+ + \phi_d$.

(C) The phase map of the actual response to the stimulus shown in Figure 2D (from a 129SV mouse, imaging time 10 min per map). The same location is stimulated at time ϕ_s^- by the reversed stimulus yielding the response at $\phi^- = \phi_s^- + \phi_d = -\phi_s^+ + \phi_d$. The relation $\phi_s^- = T - \phi_s^+ = -\phi_s^+$, where T is the period of stimulation, is justified by the cyclic nature of ϕ_s^+.

(D) The phase map of the actual response to the reversed stimulus. Both maps (C) and (D) appear to be shifted by the same hemodynamic delay ϕ_d. We call them maps of relative retinotopy. If the delay is known, the maps can be "unshifted," yielding maps of absolute retinotopy. Another way of "unshifting" the maps is subtraction of the reversed response time ϕ^- from the direct response time ϕ^+: $\phi^+ - \phi^- = 2\phi_s^+$.

(E) The magnitude of the optical response (*A* in Figure 1E), the phase of which is illustrated in (C). Gray scale below shows response amplitude as fractional change in reflection $\times 10^{-4}$.

(F) The magnitude of the optical map illustrated in (D).

(G) A map of doubled absolute retinotopy. Scale bar as in (E).

(H) Addition of the two response times ($\phi^+ + \phi^- = 2\phi_d$) gives a map of doubled delay. Uniformity of the delay map is a good indicator of suitability of the stimulus reversal method. All images show clear presence of two lateral retinotopic areas. Scale in (D) applies to all images. R, rostral; L, lateral.

should be subtracted from those to the corresponding stimuli drifting in the opposite direction.

If the system under study is sensitive to the direction of the stimulus pattern flow, the method of the stimulus reversal should not be applied. In cases like the monkey's area MT, where direction-selective cells may not respond to the stimulus moving opposite to the preferred direction (Zeki, 1974, 1980; Maunsell and Van Essen, 1983), or the song-specific cells in the songbird's area HVc, which may not respond to the same song played in reverse (Margoliash, 1983), the first strategy above should be used instead. The weak directional bias of mouse visual cortex was evident in the medial portion of V1 when responses to the vertical bars moving nasotemporally (stimulation of the contralateral eye, see Figures 2B and 2C) were compared to those moving in the opposite direction. This bias was not great enough to prevent the use of the first method.

Absolute isoelevation and isoazimuth maps of the mouse visual cortex corrected by the method of the stimulus reversal are shown in Figures 4A and 4B, respectively. Five distinct visual areas are clearly visible in the azimuth map (Figure 4B). In the area labeled V1, we see the representation extending from the periphery of the visual field (red to yellow) at its medial edge to the central visual field (green to yellow) at the border with area V2. Area V2 contains a shrunken mirror representation, going from the central visual fields where its medial edge adjoins V1 out laterally to a representation of the periphery. Lateral to V2 is another mirrored pair of areas labeled V3 and V4, the maps in which are a miniature copy of those in V1-V2. A fifth area labeled V5 and representing the periphery of the visual field is evident medial to the caudal portion of V1. The elevation map (Figure 4A) shows a single continuous representation of elevation encompassing the V1-V2 pair of areas, representing the lower visual field rostrally and the upper visual field caudally. The V3-V4 pair of areas has another continuous elevation map, and the area labeled V5 has a third one.

The organization of isoelevation and isoazimuth lines becomes apparent when contour lines that are equally spaced in the visual field are overlaid on top of the absolute retinotopic maps, shown in Figures 4C and 4D as "polar maps" in which the hue continues to encode visual field position and lightness now encodes the magnitude of the visual response (Bonhoeffer and Grinvald, 1996). The V1-V2 boundary can be identified as the longer axis of the elliptically shaped contour and corresponds to the central meridian (Figure 4D). The lateral pair of areas are clearer in Figures 3C–3H from the same mouse than in the polar plot of Figures 4C and 4D, where their smaller magnitude of response makes them darker.

A complete retinotopic map can be obtained by overlaying the isoelevation and isoazimuth sets of contour lines (Figure 4E). The two sets of contour lines are orthogonal in the V1-V2 cluster. Comparison with a composite map obtained by combining standard electrophysiological data from a large number of mice (Figure 4F, reproduced from Wagor et al., 1980) shows a very good agreement, and therefore demonstrates the power of the new paradigm. RF positions from a series of microelectrode penetrations in some cases provided additional and direct confirmation of the new maps (see Figures 7G and 7H).

The new method allows a very rapid acquisition of mouse cortical maps at high spatial resolution. A period of 2–4 min is sufficient to resolve the representations of cortical visual areas: a 100-fold reduction of the time consumed by either standard electrophysiological mapping (Wagor et al., 1980) or conventional episodic optical imaging (Schuett et al., 2002) techniques. The spatial resolution of the new technique is sufficiently reliable to resolve the internal structure of extrastriate cortical areas as small as 250 μm $\times$ 250 μm.

The lateral two extrastriate visual areas were identified reliably in 129SV mice. In C57BL/6J mice, however, the far lateral area appears to be either missing or fused with the other one (data not shown). The lateral areas in the hybrid mouse shown in Figures 4A and 4B were different in detail from both of these inbred strains, and the medial area labeled V5 in the hybrid mouse was much weaker or not evident in the 129SV strain used for Figures 3, 4C, and 4D. We have not observed any other areas in the mouse visual cortex that are organized retinotopically (observations were made in 40 C57BL/6J and 6 129SV mice).

Resolution and Reproducibility of the Mapping Procedure

A clearer appreciation of the spatial resolution of the new technique can be obtained from the plot shown in the inset to Figure 4D. This plot shows the pixel-by-pixel sequence of visual field azimuths as a function of cortical distance in V1 measured by the new procedure. The pixel size is 8.9 μm, and the magnification is 44 deg/0.7 mm or 63 deg/mm (0.016 mm/deg, in agreement with Figure 5 of Wagor et al., 1980). Despite the fact that the maps were made with completely independent calculations of topographic position at each pixel, with no smoothing of the resulting images, the plot is close to monotonic, indicating that points on the cortex separated by 20 μm have distinct visual field positions. From such plots, we estimate that the 95% confidence limits on the visual field azimuth obtained from 20 min of mapping data is 2.2° of visual angle. This is in good agreement with the error estimate calculated from the shot noise of the photosensor; this estimate of 95% confidence interval for the determination of azimuth is 3.4° of visual angle.

A second test of reliability of the new mapping procedure is to compare entire maps made at different times, rather than the pixel-by-pixel comparison within the same maps discussed in the previous paragraph. For this approach, the possibility of eye movements during imaging runs poses a problem. To test the effect of eye movements on mapping reliability, we compared topographic contour maps acquired with separation of 10 min, 1 hr, and 6 hr. Intrinsic signal images in mouse experiments typically were obtained over a period of about 6 hr, which was enough to obtain 20–30 high-quality maps. The maps separated by 10 min were basically identical. Some of the maps separated by 1 and 6 hr have uniform displacements not larger than 2°–3°, in accordance with earlier reports (Dräger, 1975; Mangini and Pearlman, 1980). Some of the maps separated by

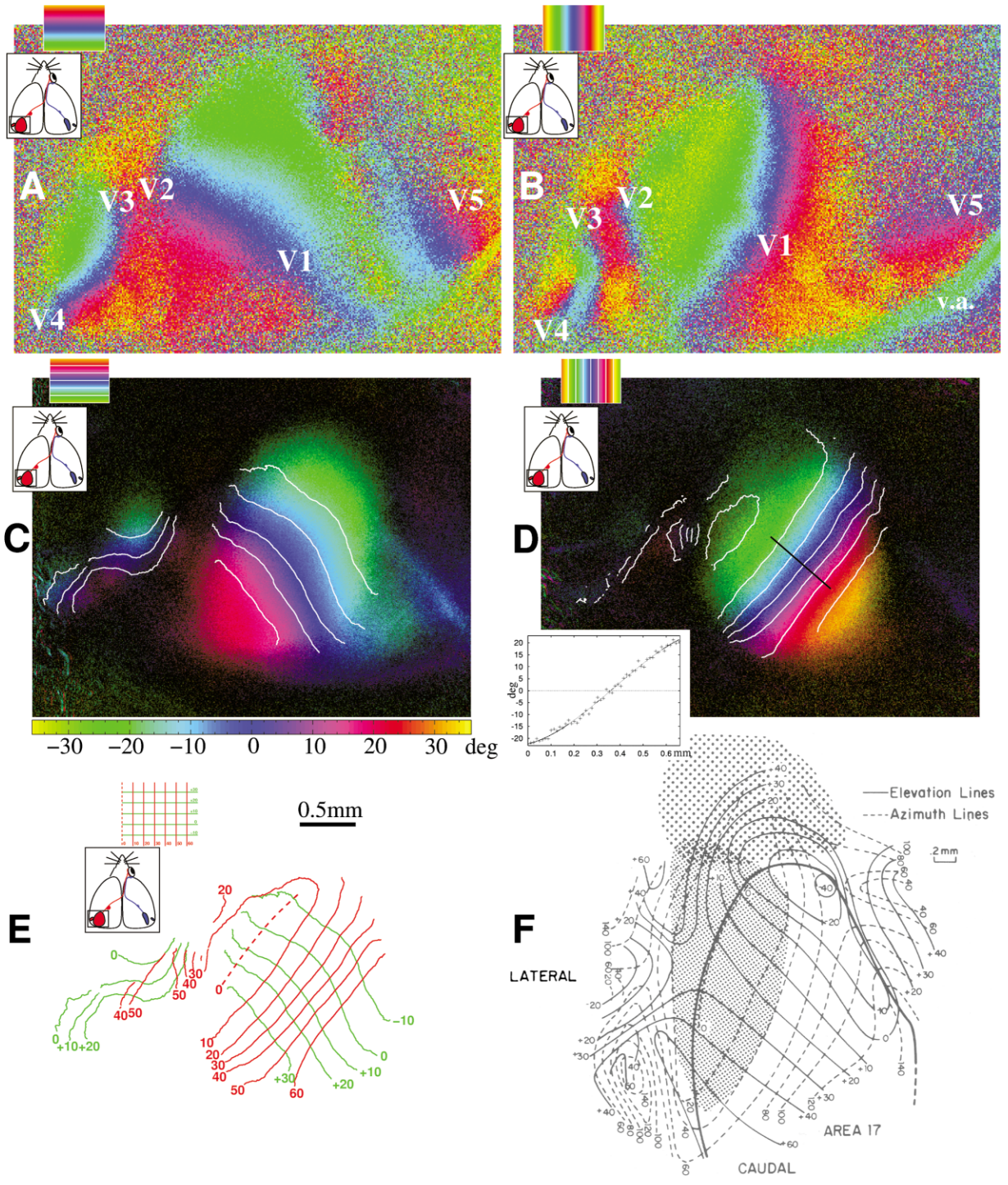

Figure 4. Maps of Multiple Visual Areas and Comparison with Electrophysiology

(A and B) Phase maps of absolute retinotopy with isoelevation and isoazimuth lines, respectively, from a hybrid mouse. Imaging time was 12 + 12 min for these maps; the delay removed by the method of the stimulus reversal. Labels V1–V5 mark topographically organized areas. v.a., vascular artifact. Supplemental movies of the temporal pattern of activation of mouse visual cortex by the stimuli used to make these maps are available at http://www.neuron.org/cgi/content/full/38/4/529/DC1.

(C and D) Polar maps of absolute retinotopy with isoelevation and isoazimuth lines, respectively, from the 129SV mouse of Figure 3. Imaging time was 10 + 10 min for these maps. The contours overlying the images have spacing of 10°; the reference contours, drawn over dark blue regions, correspond to lines running through the center of the screen (see Figures 2C and 2D). The contour lines were computed by low-pass filtering maps (using a uniform circular kernel of 5 pixels or 44 μm radius to reduce jitter) and then thresholding (at 20% of peak response amplitude to eliminate nonresponsive areas, in which phase fluctuates randomly); these contour lines were finally transferred onto the unfiltered maps. Bottom inset of (D) plots the sequence of visual field azimuths as a function of cortical distance at single pixels along the line segment shown in black.

6 hr also are stretched rather than uniformly displaced or rotated, with the result that peripheral contour lines can be displaced by as much as 5° while the central contour lines have not moved.

Comparison of Responses to the Two Eyes

So far, we have considered only responses evoked by stimulation of the eye contralateral to the imaged hemisphere, which are relatively strong because contralateral eye inputs dominate the mouse visual cortex (Dräger, 1975; Wagor et al., 1980; Mangini and Pearlman, 1980; Métin et al., 1988). Responses evoked by stimulation of the ipsilateral eye are found in the lateral one-third of V1, the so-called binocular area; RFs of the cells in this area are localized in a stripe-like zone around the central meridian: it measures about 30° in the horizontal plane and widens upward (Dräger, 1975). Within the binocular region, the cells are more likely to be driven better by inputs from the contralateral eye than from the ipsilateral one (Gordon and Stryker, 1996). Therefore, due to smaller size and weaker responsiveness, evaluation of the functional organization of the ipsilateral inputs is more challenging. There is little known about binocularity of extrastriate cortical areas. To address these issues, we stimulated monocularly not only through the contralateral but also through the ipsilateral eye in some subjects (see Figure 2A for monitor positioning).

The retinotopic maps for both eyes are presented in Figure 5 (the same subject as in Figures 4C–4E). Stimulation of the contralateral eye evoked responses in a smaller cortical region than that shown in Figures 4A and 4B because only the right half of the screen is projected onto the imaged hemisphere. As expected, responses to stimulation of the ipsilateral eye are mostly contained in the 30° region adjacent to the vertical meridian, and the activated area tapers from anterior to posterior. Note that the response color code is shifted in Figure 5B relative to that in Figure 4B since the color encoding refers to position on the monitor, and the monitor was moved from the right side of the visual field to the middle (see Figures 2A and 2B). There is no shift between color-coding of elevation in Figures 4A and 5A since the elevation of the monitor was not changed by its movement. Stimulation of the contralateral eye reveals retinotopic organization of both elevation and azimuth in the lateral secondary areas. Stimulation of the ipsilateral eye produced a clear retinotopic map of elevation in these areas (Figure 5C), revealing that the lateral areas are binocular. Responses of the lateral areas to stimulation of the ipsilateral eye with the vertical stripes used to map azimuth were present but were weaker (Figure 5D).

The contralateral isoazimuth maps clearly exhibit the reversal of the retinotopy about the central meridian (Figure 5B), which corresponds to the V1-V2 border. The ipsilateral isoazimuth maps, however, do not show the reversal (Figure 5D) or at least we could not register it. Clarification of these phenomena requires further investigation. A further peculiarity of maps activated by the ipsilateral eye in some mouse strains, evident in Figure 5D, is the apparent response to the ipsilateral visual field in an area medial to or at the medial border of V1, near its caudal edge. We hypothesize that this unusual response may represent some sort of rebound from inhibition since the area was not clearly activated on contralateral eye maps, and the phase of the response indicates activation at a time when the stimulating stripes were not present in the binocular field and, thus, could not stimulate the eye. It is also possible that misdirected callosal inputs are responsible for exciting these responses (Olavarria and Montero, 1989).

Since the responses to stimulation of the ipsilateral eye had clearly defined retinotopic organization, we attempted to test how well they match with those to stimulation of the contralateral eye. Topographic contour maps, analogous to one shown on Figure 4C, were constructed and overlaid one on top of the other. A simple comparison revealed that the maps are very similar, not shifted, but rotated by 9° (the ipsilateral map was rotated counterclockwise relative to the contralateral map). To elucidate this disagreement, we carried out the matching analysis for two more subjects. Maps of one of them were again similar, shifted by only 2°–3° and rotated by 11° in the same relative direction. Maps of the other subject were similar and well aligned. We interpret this as suggesting that the eyes have a tendency to droop under the conditions of this experiment, that is, to be rotated in the coronal plane by up to 5°. Rotations in the other two planes (horizontal and sagittal) are insignificant. This tendency can be caused by anesthesia and/or by the surgical procedure, which requires displacement of the scalp to gain access to the skull surface.

The results above were obtained by exposing one hemisphere and imaging it at high resolution using monocular stimulation. We also imaged both hemispheres simultaneously at lower resolution through the intact skull, using both monocular and binocular stimulation (Figure 6). These maps clearly reveal the partition of the visual field between the two hemispheres and the relative dominance of the two eyes in each. This minimally invasive procedure allows one to evaluate visual responses in a region of interest before and after deprivation in the same subject or simply to monitor changes during development. Responses to binocular stimulation were typically stronger than those to either eye stimulated alone, and were sometimes as great as the sum of the separate monocular responses. Responses in V1 to the contralateral eye were usually about twice as strong as those to the ipsilateral eye.

(E) The organization of isoelevation (green) and isoazimuth (red) lines in the mouse visual cortex. The reference contours (0° contours) correspond to the horizontal (green) and vertical meridians (red). The contours were obtained by the procedure outlined above from the maps shown in (C) and (D). Not all contour lines drawn over the primary areas are present over the secondary area since the latter have weaker responses than the former.

(F) Composite retinotopic map (21 mice) constructed using standard electrophysiological mapping technique from Wagor et al. (1980), published with permission.

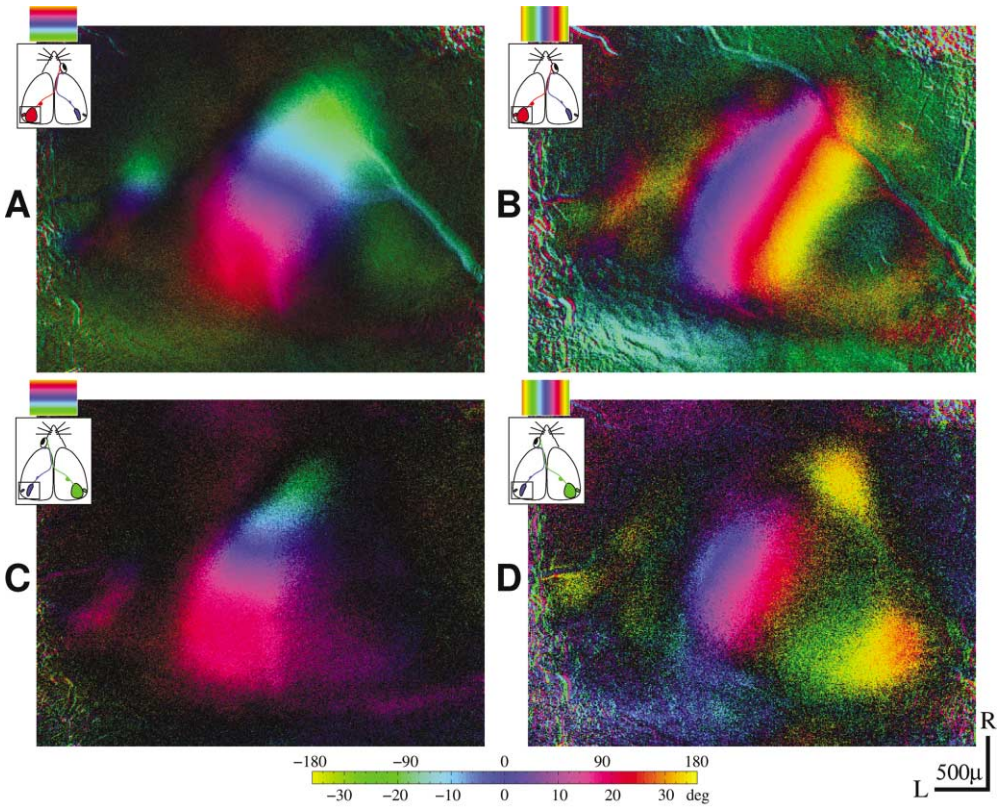

E

	Elevation			Azimuth		
	P	SL	SM	P	SL	SM
Contralateral	2.2	0.9	0.6	1.8	0.5	0.4
Ipsilateral	1.1	0.5	0.4	0.8	0.3	0.7

Figure 5. Comparison of Responses Evoked by Stimulation of Eyes Contra- and Ipsilateral to Imaged Hemisphere

(A and B) Contralateral isoelevation and isoazimuth retinotopic maps, respectively.

(C and D) Ipsilateral isoelevation and isoazimuth retinotopic maps, respectively.

(E) The table summarizes peak fractional change (PFC) of reflectance ($\times 10^{-4}$) for different areas. Peak response of the stronger of the two lateral areas is tabulated. Isoazimuth stimulation of the ipsilateral eye evoked strong nonretinotopic response anterior V1 (0.6×10^{-4} PFC). Activation of this area was reliably identified on two other independent maps (not shown here). This area appears fused with V1 or silent in other maps. Noise level is 0.15×10^{-4}. Convention as in Figures 2 and 3. P, primary; SL, secondary lateral; SM, secondary medial.

Confirmation of Maps Using Spatially Restricted Stimuli

The maps above have all been constructed using temporally encoded stimuli. For example, in the case of the stimulus used to map elevation, a horizontal low duty-cycle square-wave grating drifting vertically, the reconstruction of retinotopy relied on the time at which the reflected light response was greatest. From the temporal phase of the response, we have calculated the temporal phase of the stimulus giving rise to that response, which in turn determines the spatial position of the stimulating elements (in this case, a white stripe). A similar experiment was carried out to determine azimuth using vertical stripes.

An alternative approach is to use spatially encoded stimuli. If the stimulus is confined to a small region of the visual field, the cortical responses are centered on the area that corresponds visuotopically to the stimulus (Das and Gilbert, 1995; White et al., 1999; Bosking et al., 2000, 2002; Schuett et al., 2002). The correspondence between a spatially encoded stimulus and the locus of the cortical response is independent of the details of hemodynamics or assumptions about latency; hence, such maps can provide an independent confirmation of the much more detailed maps derived using temporally encoded stimuli.

We confirmed the maps obtained by the temporally encoded stimuli (Figures 7A and 7B) using a hybrid stimulus: a circular spot that moved periodically across the visual field along a vertical or horizontal straight line at the 0° isoazimuth or isoelevation line. This stimulus is confined spatially in one of the two spatial dimensions, and the response map of this dimension is encoded spatially. The other dimension is encoded temporally. Figures 7C and 7D show the responses to the spots, which are consistent with the azimuths (Figure 7C) and elevations (Figure 7D) determined from the temporally encoded maps. Transferring contour lines from the iso-

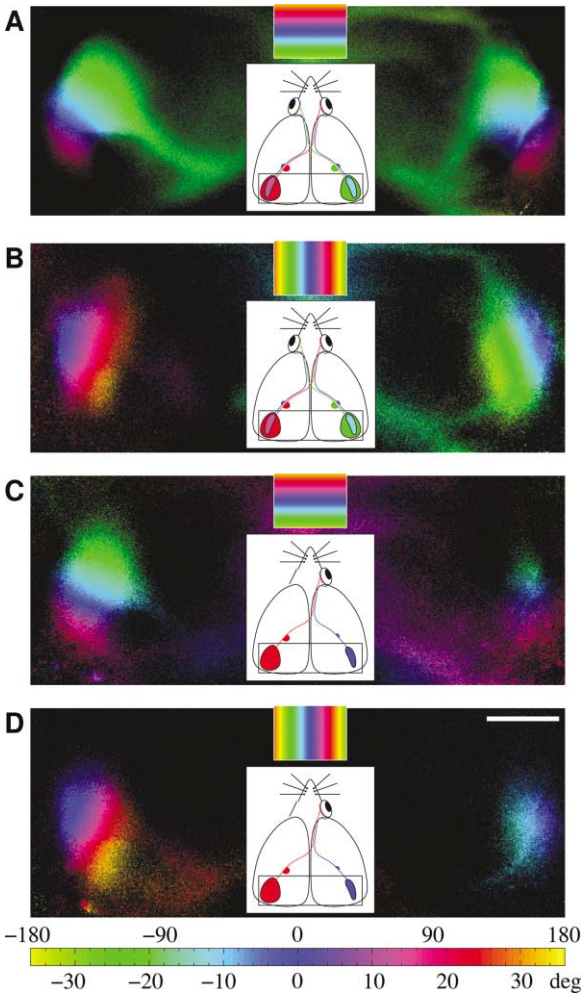

Figure 6. Imaging Both Hemispheres Simultaneously through Intact Skull

(A and B) Binocular isoelevation and isoazimuth retinotopic maps, respectively.

(C and D) Right eye isoelevation and isoazimuth retinotopic maps, respectively. The left eye maps are not shown. Scale bar equals 1 mm.

azimuth map (Figure 7A) to the map obtained with vertically drifting spots (Figure 7C) and from the isoelevation map (Figure 7B) to the map obtained with horizontally drifting spots (Figure 7D) shows that the zero-degree contour lines fall directly to the centers of the activated areas, thus proving that the results obtained with the two methods of stimulation are equivalent. This can be seen even more clearly on thresholded pictures (Figures 7E and 7F), in which only the strongest responses are colored.

Despite the fact that the circular spots (4°) were much smaller than the length of the stripes that constituted the gratings (62° for vertical gratings and 77° for horizontal one), the maps obtained with the spots (Figures 7C and 7D) appear fairly similar to those made using gratings drifting in the corresponding directions (Figures 7A and 7B). The size of the primary cortical area activated by the full-screen stripes is only about twice as large as that activated by the small spots, and activation of the secondary areas is about the same. The large extent of the cortical activation (30°–40°) by a minimal visual stimulus can be attributed partly to the fact that RF size in the mouse primary cortex can be as large as 30° in diameter, or even larger (Mangini and Pearlman, 1980; Métin et al., 1988). The majority of the RFs defined by extracellular recording are between 10° and 20°, averaging at about 15° (these estimates are the means of the major and minor axes of the RFs). However, neurons in the upper cortical layers tend toward smaller RF sizes, generally less than 12° (Métin et al., 1988). Our less exhaustive study (Figure 7G) showed that the sizes of multiunit RFs in V1 were about 20° in the region close to the vertical meridian and about 30°–40° in the periphery. The convolution of the 4° stimulus with a 15° RF would give rise to a swath of activation no more than the representation of 19° on the cortex, while the area actually activated occupies the cortical representation of 30°–40° even near the vertical meridian. Therefore, subthreshold activation of cortical neurons probably makes a major contribution to the optical "point spread" (Das and Gilbert, 1995). Our estimate for the mouse primary visual cortex is that the activity below 70% of the peak optical response should probably be attributed to the subthreshold activation, since this threshold gives activation area of a size comparable with the average RF size (15°) augmented by the size of the stimulus elements (4°).

Confirmation of Maps Using Electrophysiology

Further confirmation of the optical maps of retinotopy was obtained using conventional microelectrode recording. After acquisition of the image of the surface vasculature and optical maps, we performed a series of electrode penetrations in V1 mainly along rostrocaudal and mediolateral rows. The electrophysiological RFs were hand mapped on a glass screen positioned at the location of the stimulus monitor (see Figure 2B); thus, the RFs were mapped on the same physical surface in the two cases to allow direct comparison. Figure 7G shows the RFs mapped by electrophysiology in relation to the topographic position determined from optical imaging. There was a close match between the two, with the position within each RF giving the strongest multiunit response in no case more than 5° from the topographic position determined from optical imaging. Figure 7H demonstrates the excellent correlation between RF azimuths and elevations obtained by the two techniques, with an R value of 0.98.

Orientation Maps in Cat Visual Cortex

As a final test of the validity and efficiency of the new paradigm for optical imaging, we have employed it to map orientation columns in cat visual cortex. Optical imaging using the traditional approach has been successful in revealing the structure of the domains of orientation preference in visual cortices of higher mammals (Blasdel and Salama, 1986; Bonhoeffer and Grinvald, 1991). Figure 8 shows that the new paradigm makes orientation maps much more quickly and with much less variability; the validity of these maps is confirmed by those obtained using the longer, noisier, traditional procedure. With the new method, we can obtain high-qual-

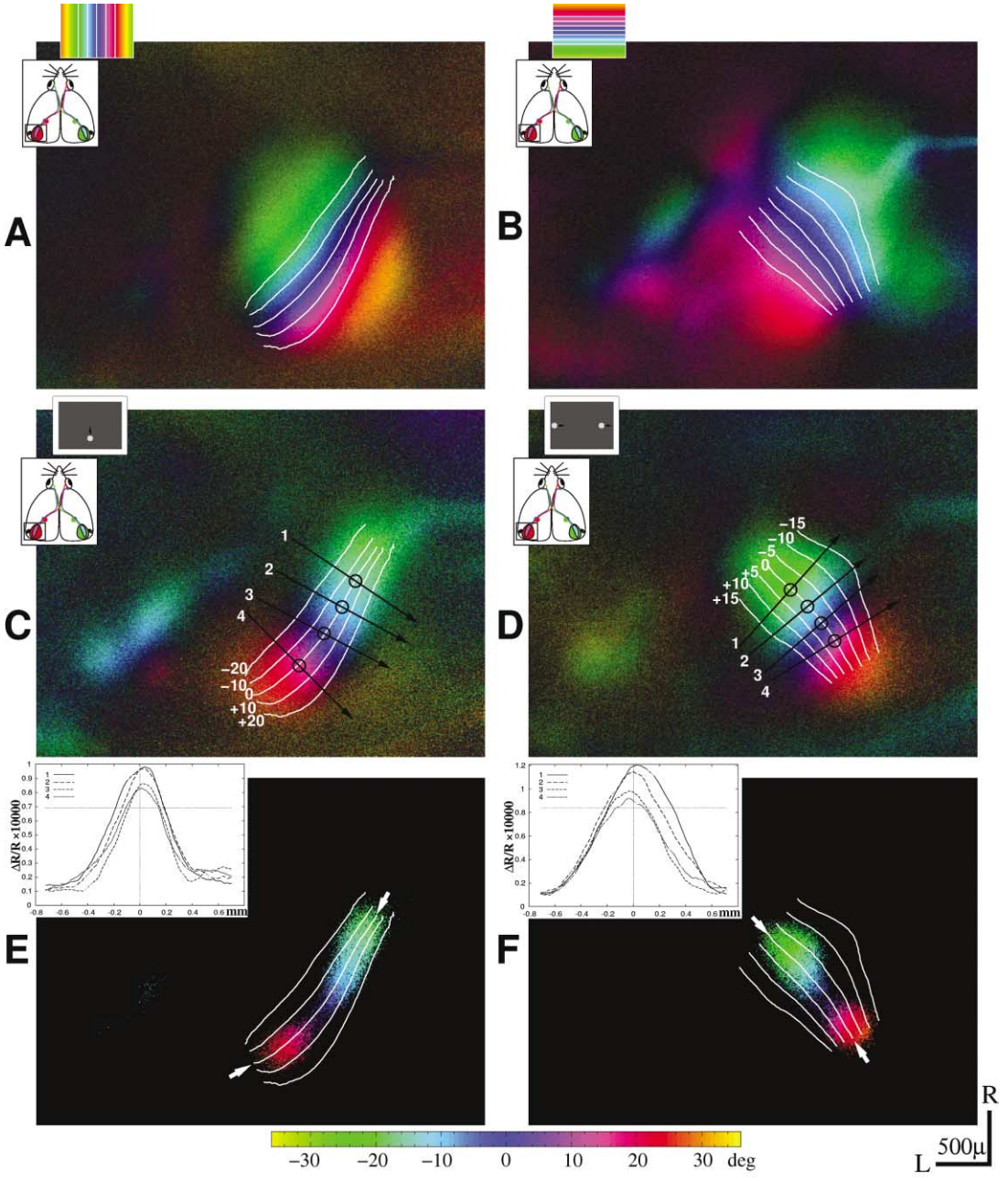
A
B
C
D
E
F
1
2
3
4
−20
−10
0
+10
+20
−15
−10
−5
0
+5
+10
+15
ΔR/R ×10000
mm
R
L
500μ
−30 −20 −10 0 10 20 30 deg

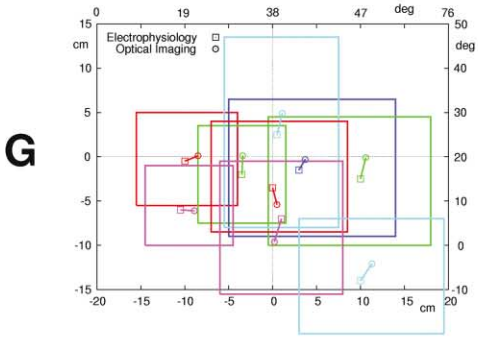
G
Electrophysiology
Optical Imaging
cm
deg

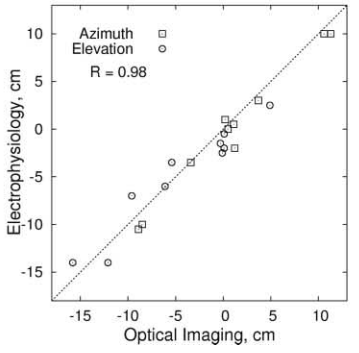
H
Azimuth
Elevation
R = 0.98
Electrophysiology, cm
Optical Imaging, cm

ity orientation maps in as little as 1 min (Figure 8A). This is at least a 28-fold acceleration of map acquisition, as compared to the conventional procedure, without compromise of spatial resolution or quality. The map computed from 4 min of imaging using the new paradigm (Figure 8C) is almost perfectly smooth despite the complete absence of any smoothing in the computations that produced the map.

Discussion

This paper describes a new approach to intrinsic signal optical imaging of sensory maps using a continuous, temporally encoded, periodic stimulus; continuous image acquisition; and Fourier analysis for extraction of responses. We show that the new method is vastly more efficient than traditional approaches at producing maps of orientation columns in the cat, and we use it to delineate as many as five visual areas in the cortex of the mouse with extreme cortical and topographic resolution. We discuss below the sources of the improvement in quality and efficiency, the new experimental findings on visual cortical organization in mouse, and the other systems to which this approach has been applied in preliminary work.

Examination of Sources of Improvement

The improvement of the optical mapping reported in this paper can be ascribed to three sources: advanced imaging hardware, new methodology, and continuous stimulation.

First, we have taken advantage of the progress in the computer and imaging technologies of the past decade. Modern frame transfer CCD cameras have very high data rates (40 MHz from a single output and higher), which can provide either continuous high-resolution imaging (1024 $\times$ 1024 pixels per image and higher) or ultra high-speed episodic imaging (1,000,000 fps in burst mode). Current computer technology matches these high data rates by offering massive storage devices to save the data stream and very fast computation units to analyze it. The higher data rate allows one either to sample stimulus parameter space more densely or to utilize it toward better averaging, thus reducing shot noise. For example, upgrading from the Pentamax-based system (5 MHz data rate) to the Dalsa-based one (40 MHz data rate) yielded an almost 3-fold reduction in the map acquisition time without compromise of map quality.

Second, the conventional approach relied on blind averaging of responses to many repetitions of each stimulus distributed over the 15–90 min time course of each experimental run. This averaging procedure inadvertently mixed the evoked response with slow activity and other artifacts. Because many of these artifacts are spatially uniform over cortical distances exceeding 1 mm, they can be removed by the filtering with a kernel of appropriate size (e.g., 2–3 mm) without distorting the pattern of orientation columns, the period of which is less than 1 mm. If there were a real functional structure as large as the filter kernel, it would also be removed by this procedure.

In the new approach, frames are saved without or with only small temporal binning, offering the full-time series for further processing and analysis. As a first stage, we used an acausal temporal high-pass filter independently on each pixel to remove the slow activity and leave the evoked responses and the high-frequency artifacts intact. These filters used a window size of at least two full stimulus cycles in the case of periodic stimulation and of at least six durations of one condition presentation in the case of episodic stimulation. If the episodic stimulation is in use, the frames are averaged according to their stimulus condition, and consequently some artifacts are still mixed with the evoked response. These artifacts can be partially removed by temporal low-pass filtering. Better results are achieved if the continuous-periodic stimulation is employed. Then we carry out another stage of processing: extracting the phase and amplitude of the Fourier component at the frequency of stimulation, thus effectively removing the rest of artifacts. The phase gives us time of the response, which is used to find state of the stimulus (equivalent to the stimulus condition if we were using episodic stimulation), and the amplitude is interpreted as a magnitude of the response. Finally, spatial high-pass filtering can be applied if a map's quality is inadequate, although we have found this not to be necessary when using continuous-periodic stimulation. For mouse imaging, we have not used spatial filtering at all. We have, in some cases, removed a DC bias.

Third, the effective removal of the high-frequency artifacts when using continuous-periodic stimulation is not

Figure 7. Comparison of Retinotopic Maps Obtained by Temporal and Spatial Stimulus Encoding and Electrophysiology

(A and B) Polar maps of absolute isoazimuth and isoelevation retinotopy, respectively. Stimulus: full-screen bars drifting horizontally (A) and vertically (B) in the right visual hemifield, as in Figures 2B–2D. The contours overlying the images have spacing of 10° and 5° for (A) and (B), respectively. Contour lines were constructed using the procedure described in the caption to Figure 4.

(C and D) Polar maps of absolute isoelevation and isoazimuth retinotopy, respectively, mapped using 4° circular spots drifting vertically (C) and horizontally (D). The trajectories of the spots pass through the center of the screen; monitor position is identical to that for (A) and (B). Using smaller spots (2°) led to drastic reduction of responses. The contours overlying the images are transferred from maps shown on (A) and (B), respectively.

(E and F) Polar maps of (C) and (D), respectively, after thresholding at 70% of the peak response. The arrows mark the contour lines corresponding to the trajectories of the spots: the zero-degree lines passing through the center of the screen. Insets of (E) and (F) are average curves (5 pixel kernel radius) of the cuts through maps shown on (C) and (D), respectively. The cuts have their centers aligned with the corresponding central contours and are orthogonal to those. Threshold at 70% indicated by horizontal lines.

(G) Comparison of electrophysiological RFs with those defined by optical imaging mapped on the same physical surface (subject different from A–F). The dimensions of the plot correspond to the dimensions of the stimulus monitor screen (bottom and left) (Figure 2D) and to degrees of the visual field (top and right) (Figures 2B and 2F).

(H) Correlation between electrophysiological and imaging for both azimuths and elevations of the RFs shown in (G). Conventions as in Figure 3.

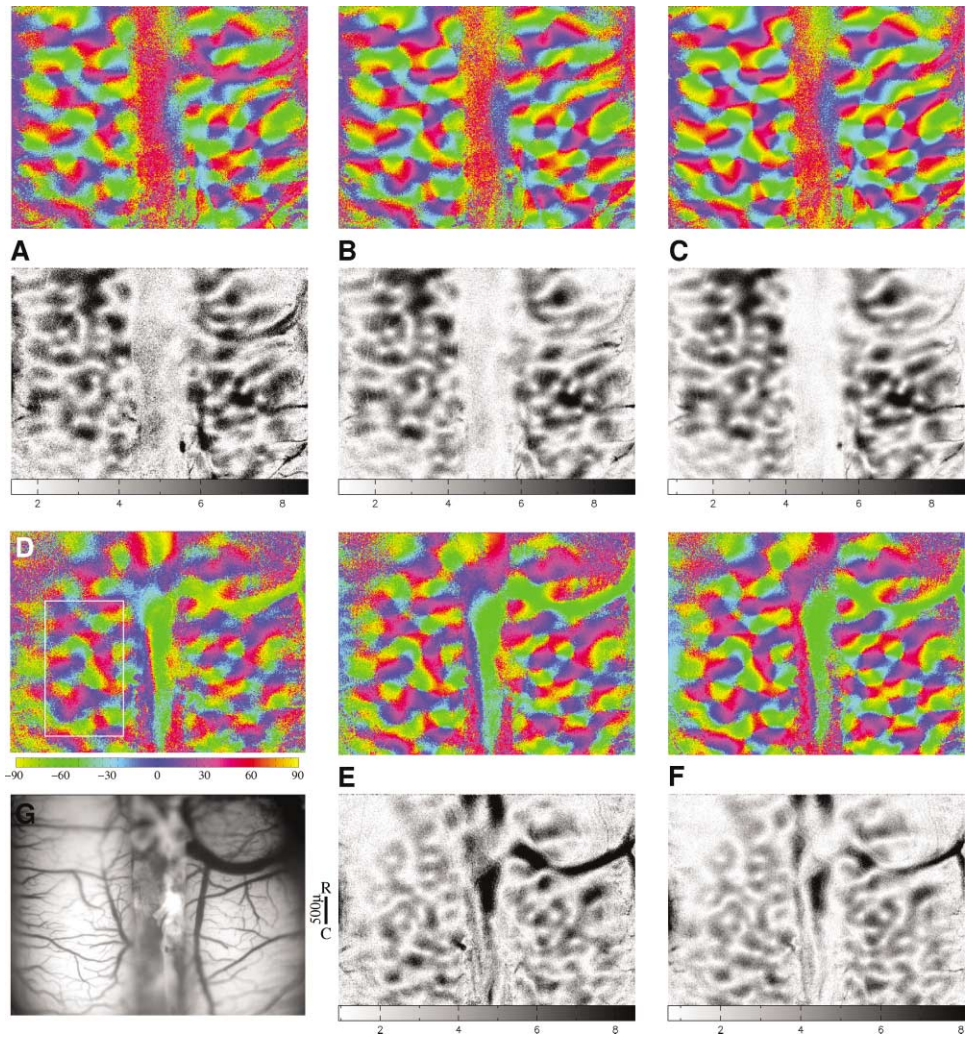

Figure 8. Comparison of Orientation Maps Obtained by the New Continuous-Periodic Imaging Paradigms with Conventional Maps from the Same Cortex

(A–C) Phase (color, above) and magnitude (grayscale, below) maps obtained utilizing the continuous-periodic stimulation (1 min/cycle, see Figure 2G) and continuous acquisition paradigm. These orientation maps show the phase and magnitude of the second harmonic response (30 s/cycle, 360°/min rotation), since one full rotation of the stimulus pattern (Figure 2G) has two cycles of orientation. Imaging time was 1, 2, and 4 min for (A), (B), and (C), respectively.

(D–F) Phase and magnitude maps obtained utilizing the standard episodic stimulation (see Experimental Procedures) and continuous acquisition (only the phase map is shown in D). Imaging time was 1, 2, and 4 blocks (1 block = 28 min or 16 stimulus repetitions) for (D), (E), and (F), respectively. The maps were temporally (time window of 120 s for A–C and of 67 s for D–F) and spatially (uniform circular kernel of 70 pixels or 1.5 mm radius) high-pass filtered. Quality of maps within the region outlined in (D) (20,900 pixels) was evaluated in two ways: first, by the correlation *between* each pixel in the test map and the corresponding pixel in a reference map (*b*), which was an 8 min map obtained by continuous-periodic imaging (not shown); and second, by the correlation between neighboring pixels *within* each individual test map (*w*). As is evident by eye, these measures of map quality were much higher for continuous-periodic imaging than for episodic imaging, and they improved with increases in imaging time in both paradigms (A: $b = 0.925$, $w = 0.889$; B: $b = 0.966$, $w = 0.938$; C: $b = 0.987$, $w = 0.968$; D: $b = 0.712$, $w = 0.832$; E: $b = 0.758$, $w = 0.796$; F: $b = 0.771$, $w = 0.927$). Quality of all maps was distinctly improved by the temporal filtering. Improvement of map quality by high-pass spatial filtering was small (*b* values) for (A) (from 0.835 to 0.925), smaller for (B) and (C) (from 0.879 to 0.966 and from 0.939 to 0.987, respectively), but major for (D)–(F) (from 0.217 to 0.712, from 0.281 to 0.758, and from 0.481 to 0.771, respectively). Comparison among independent 1 min continuous-periodic runs like (A) yielded correlations of 0.858, while comparisons among independent 28 min episodic runs like (D) yielded lower correlations of 0.750.

(G) The vascular pattern in the region of cortex imaged. The gray stripe in the middle is reflected dura. Conventions as in Figure 3.

the only advantage of the new paradigm. Time is saved simply because continuous stimulation does not require interstimulus relaxation intervals (typically 50% of the time with discrete stimulation protocols). A final important benefit of the new paradigm is of a neurobiological nature: continuous stimulation samples stimulus parameter space very densely (almost continuously in practice), as a result, it assures uniform neural activation. For example, with a standard 4- or 8-orientation sampling protocol (45° or 22.5° intercondition spacing), many well-tuned neurons will be weakly activated, or not activated at all, because their preferred orientation is not sufficiently close to one of the stimulated orientations.

Lastly, use of the new methodology led to significant

simplification of the imaging hardware. Straightforwardness of the new mapping method and simplicity of the imaging system design should benefit not only the neurophysiological imaging community but also researchers from other areas of neuroscience who need high-resolution, rapid evaluation of cortical functions.

Comparison with Results from Traditional Optical Imaging

It is useful to compare findings from the new paradigm with those obtained using traditional approaches to intrinsic signal optical imaging. The traditional approach applied to mouse visual cortex (Antonini et al., 1999; Schuett et al., 2002) can map responses to at most 20–30 distinct stimuli. For example, topography was evaluated at 21 points in Schuett et al. (2002). These responses provide the only real data from this approach, and any appearance of finer structure is the result of an interpolation procedure that is guaranteed to be misleading at borders between distinct areas. The published episodic optical maps of mouse cortex seem unlikely to portray topography accurately, since in half of the cases examined, the electrophysiological maps differed from the optical maps by 35° or more (Figure 4B in Schuett et al., 2002). In contrast, the measurements of precision detailed above demonstrate that the new method described here can determine topographic position at no fewer than 800 distinct positions within V1. Each of these data points represents a genuine, independent measurement of the visual field representation. The use of spatially encoded stimuli (Figures 7A–7F) and microelectrode recording (Figures 7G and 7H) confirm the accuracy of the new optical maps at this level of precision (with a maximum difference between electrophysiology and imaging of less than 5° and an average difference less than 3°). The new paradigm therefore yields an approximate 40-fold improvement in areal resolution.

The time needed to obtain maps using the new paradigm is also dramatically improved, again by a factor of more than 30, and in many cases more than 100. Maps of equivalent quality were obtained from cat visual cortex in approximately 1/50th the time. Topographic maps in mouse visual cortex with 40-fold higher resolution than those in Schuett et al. (2002) could be obtained in less than 1/30th the time.

Finally, the new paradigm permits independent, high-resolution maps to be obtained rapidly from individual animals, making the approach useful in studies of transgenic or experimentally altered animals, in which measurements must be obtained from single individuals that might be different from one another. It should be noted that the highest-resolution maps in Figures 2, 3, and 5 of Schuett et al. (2002) present data from maps that have been averaged across subjects and are therefore not suitable for comparing data from individuals.

Summary of New Experimental Results

High-resolution maps obtained by the use of the new paradigm have revealed fine details of the mouse visual cortex. In addition to the known retinotopy of the primary and secondary visual cortex, we also observed retinotopic organization in a pair of more lateral visual areas. Both of these areas appear to be binocular. It is possible that each of the lateral areas has further subdivisions. An additional retinotopic area medial to V1 was identified in some strains; it appears to be only weakly retinotopic in others. There were also signs of an area anterior to V1 in some cases.

A small visual stimulus evoked optical responses over a large region of V1 and V2. This is consistent with the overall poor feature selectivity of mouse visual cortex and with a large cortical point-spread function. The lateral visual cortical areas showed strong preference for horizontal over vertical drifting bars, and peripheral V1 showed weak directional asymmetry for horizontal movement. Stimulation with drifting-rotating bars or gratings, however, which were very effective in studying orientation selectivity of cat primary visual areas, failed to reveal local clustering of responses in mice, consistent with microelectrode studies (Dräger, 1975; Mangini and Pearlman, 1980). These two facts indicate that mice may have a global rather than a local mechanism of orientation/direction selectivity. That is, rather than having different columns within an area, some secondary areas may be used for detection of motion in certain orientations or directions.

Comparison with Anatomically Defined Areas

We refrain from identification of the functional areas mapped in this paper with the anatomical ones described earlier (Olavarria et al., 1982; Olavarria and Montero, 1989) for a variety of reasons. First, most of the information on the cortical visual areas of the rodent comes from the rat, and there are relatively few anatomical studies of higher visual cortical areas in the mouse. Indeed, even the locations of V1 shown in mouse atlases are extrapolated from the rat. Maps of the rat visual areas with the techniques reported in this paper are clearly different from those of the mouse (data not shown). Second, there are consistent differences in the organization of the secondary areas among different mouse strains. For example, we have observed only one lateral secondary area in C57BL/6J mice. Third, some mismatch between anatomical and functional maps would be expected to result from peripheral abnormalities. For example, the C3H strain that was used for normal anatomical studies of connections to and among visual cortical areas (Olavarria et al., 1982) is now known to carry the retinal degeneration allele *rd* (Williams et al., 1996). This strain loses nearly all photoreceptors by 2 months of age. We found extreme deterioration of visually evoked responses in these mice as well. Finally, in earlier anatomical tracer studies, the topographic positions of injection and projection sites within the maps of each visual area were not known, making the assignment of areal designations problematic. For example, tracer injections away from the V1-V2 border might be expected to label twice the number of projection sites as those at the border. Use of the mapping technique presented in this paper should make a precise and unified anatomical/functional classification feasible.

Other Applications and Future Directions

In addition to the results reported in this paper, we have obtained high-resolution maps in various cortices of different species: mouse, visual cortex (retinotopy), auditory cortex (tonotopy); rat, visual cortex (retinotopy), au-

ditory cortex (tonotopy, presented in V.A. Kalatsky and M.P. Stryker, 2002, Soc. Neurosci., abstract); and ferret and cat, visual cortex (retinotopy, orientation and direction selectivity). The method has proven to be very effective in identifying functional abnormalities in visual and auditory cortices of mutant mice. Applications of the proposed technique and optical imaging system are not limited to the cortical regions and species noted above. In particular, we expect the new method to be useful for optical imaging of the brain of awake, behaving primates. Since the new method saves the entire, continuous sequence of image frames, it should be possible to compensate fully for movement artifact, which would be impossible if only the averaged images were saved as in the conventional approach. In addition, the removal of the slow component makes it possible to piece together a periodic response from a sequence of responses that were acquired discontinuously in individual trials. Finally, many useful stimuli, including the visual stimulus that we have used for orientation maps, do not require precise control of fixation, and therefore can be used for periodic mapping over periods much longer than a typical alert animal fixation trial. The same methodology should be applicable to intraoperative mapping of the human brain.

Experimental Procedures

Surgical Preparation

The surgical preparation and maintenance procedures are similar to those described previously (Gordon and Stryker, 1996; Issa et al., 2000). All experimental procedures were approved by the UCSF Committee on Animal Research.

Mice (129SV from Charles River Labs, C57BL/6J from BNK, C3H from Simonsen Labs, and hybrid C57Bl6-Icr-129J bred locally) were anesthetized with an intraperitoneal injection of urethane (1.0 g/kg in 10% saline solution) or pentobarbital (50–90 mg/kg). A sedative, chlorprothixene (0.2 mg/mouse i.m.), was administered to supplement urethane. Additionally, lidocaine (2% xylocaine jelly) was applied locally to all incisions. Atropine (5 mg/kg in mouse) and dexamethasone (0.2 mg/mouse) were injected subcutaneously. The atropine was necessary to reduce secretions and to counter the parasympathomimetic effect of the anesthetic agents; the dexamethasone helped avert cerebral edema. The animal's temperature was maintained at 37.5° by a rectal thermoprobe feeding back linearly to a heating pad on which the animal rested throughout the experiment. A tracheotomy was performed and electrocardiograph leads were attached to monitor the heart rate continuously throughout the experiment. Mice were placed in a stereotaxic instrument aligned with the stimulus monitor as shown in Figures 2A and 2B. Because the mouse lacks a fovea or an area centralis that can be plotted ophthalmoscopically, we followed the approach of earlier investigators of visual cortical topography in the mouse (Wagor et al., 1980) and defined topographic positions with respect to the head, with the vertical meridian taken to be the extension of the midsagittal plane and the horizontal meridian taken to be the projection of the height of the eyes when the skull was level between lambda and bregma. A craniotomy was made over the area of interest; the dura mater was left intact. In some mice, the skull was left intact as well. Low-melting point agarose (3% in saline) and a glass coverslip were placed over the exposed area.

Cats were initially anesthetized with the inhaled anesthetic isoflurane (3%–4% in O_2) and, after implantation with a femoral catheter, were switched to a short-lived barbiturate (thiopental, 20–30 mg/kg). Atropine (0.04 mg/kg) and dexamethasone (1.0–2.0 mg/kg) were injected subcutaneously to reduce tracheal secretions and minimize the stress response, respectively. A tracheotomy was performed, and a long-lasting barbiturate (sodium pentobarbital) was substituted for thiopental. To assess the anesthetic state of an animal, we continuously monitored its core temperature, electrocardiogram, expired CO_2, and peak airway pressure. A feedback-regulated heating pad maintained core body temperature at 37.5°. Pentobarbital was administered as needed to keep the animal at a surgical plane of anesthesia, determined by the animal's reflexes, heart rate, and peak expired CO_2. The animal was placed in a stereotaxic apparatus and ventilated with nitrous oxide:oxygen 2:1. 1% atropine sulfate and 10% phenylephrine hydrochloride were applied to the eyes. To focus the eyes on the stimulus monitor, contact lenses of the appropriate strength were fitted with the aid of a retinoscope. A craniotomy was made over the lateral gyrus of both hemispheres. Neuromuscular blockade was then induced by continuous infusion of pancuronium bromide (0.08–0.2 mg/kg/hr) mixed in 2.5% dextrose in lactated Ringer's solution (total volume of fluid infused, 5–10 ml/kg/hr), and ventilation was continued for the duration of the experiment. After neuromuscular blockade, anesthesia was delivered at a rate that maintained heart rate and peak expired CO_2 at their values prior to the blockade. The dura mater was reflected, and low-melting point agarose (3% in saline) and a glass coverslip were placed over the exposed cortex.

Imaging Procedures

Optical images of cortical intrinsic signal were obtained using Dalsa 1M30 CCD camera (Dalsa, Waterloo, Canada) or Pentamax-EEV 576x384 CCD camera (Roper Scientific, Inc., Tucson, AZ) controlled by custom software. Using different tandem lens configurations (Nikon, Inc., Melville, NY), "low-resolution" (50 $\times$ 50 mm lenses, 6.4 $\times$ 8.4 mm image area [Pentamax]), "medium-resolution" (85 $\times$ 50 mm lenses, 7.2 $\times$ 7.2 mm image area [Dalsa]), and "high-resolution" (135 $\times$ 50 mm lenses, 4.6 $\times$ 4.6 mm image area [Dalsa]) images could be acquired. The surface vascular pattern or intrinsic signal images were visualized with illumination wavelengths set by a green (546 $\pm$ 10 nm) or red (610 $\pm$ 10 nm) interference filter, respectively. After acquisition of a surface image, the camera was focused 400–500 μm below the pial surface, an additional red filter was interposed between the brain and the CCD camera, and intrinsic signal images were acquired. Frames were acquired by 1M30 camera at the rate of 30 fps and were stored as 512 $\times$ 512 pixel images after binning the 1024 $\times$ 1024 camera pixels by 2 $\times$ 2 pixels spatially and by 4 frames temporally, reducing sampling rate for the stored images to 7.5 Hz and increasing well depth to 16 bit. Frames were acquired by Pentamax camera at the rate of 20 fps and were stored as 384 $\times$ 288 pixel images after temporal binning by 4 or 16. Images were analyzed using custom software.

Visual Stimuli

Drifting bars, drifting-and-rotating full-field square-wave gratings, and drifting circular spots were generated by a Matrox G450 board (Matrox Graphics, Inc., Quebec, Canada), controlled by custom software, and displayed on a high refresh rate (1024 $\times$ 768 @ 120 Hz) monitor (Nokia Multigraph 445X). For episodic stimulation, drifting full-field square-wave gratings with a fundamental spatial frequency of 0.2 cycles per degree and a temporal frequency of 2.0 cycles/s were used. The gratings were presented in pseudorandom order separately to the two eyes at eight orientations separated by 22.5°, and were interspersed with four identical blank screen conditions viewed by both eyes, for a total of 20 stimulus conditions.

Acknowledgments

We thank Sharif Taha and Naoum Issa for their assistance with experiments and for constructive discussions, and Marcos Frank and Patrick McQuillen for comments on the manuscript. V.A.K. is a Sloan-Swartz Fellow in Theoretical Neuroscience. This work was supported by a UCSF Sandler Award in Basic Science and by grants from the NIH to M.P.S. (EY02874 and NS16033).

Received: October 18, 2002
Revised: February 3, 2003
Accepted: April 28, 2003
Published: May 21, 2003

References

Antonini, A., Fagiolini, M., and Stryker, M.P. (1999). Anatomical correlates of functional plasticity in mouse visual cortex. J. Neurosci. *19*, 4388–4406.

Blasdel, G., and Campbell, D. (2001). Functional retinotopy of monkey visual cortex. J. Neurosci. *21*, 8286–8301.

Blasdel, G.G., and Salama, G. (1986). Voltage-sensitive dyes reveal a modular organization in monkey striate cortex. Nature *321*, 579–585.

Bonhoeffer, T., and Grinvald, A. (1991). Iso-orientation domains in cat visual cortex are arranged in pinwheel-like patterns. Nature *353*, 429–431.

Bonhoeffer, T., and Grinvald, A. (1996). Optical imaging based on intrinsic signals—the methodology. In Brain Mapping: The Methods, A.W. Toga and J.C. Mazziotta, eds. (New York: Academic Press), pp. 55–97.

Bosking, W.H., Kretz, R., Pucak, M.L., and Fitzpatrick, D. (2000). Functional specificity of callosal connections in tree shrew striate cortex. J. Neurosci. *20*, 2346–2359.

Bosking, W.H., Crowley, J.C., and Fitzpatrick, D. (2002). Spatial coding of position and orientation in primary visual cortex. Nat. Neurosci. *5*, 874–882.

Boynton, G.M., Engel, S.A., Glover, G.H., and Heeger, D.J. (1996). Linear systems analysis of functional magnetic resonance imaging in human V1. J. Neurosci. *16*, 4207–4221.

Daniel, P.M., and Whitteridge, D. (1961). The representation of the visual field on the cerebral cortex in monkeys. J. Physiol. *159*, 203–221.

Das, A., and Gilbert, C.D. (1995). Long-range horizontal connections and their role in cortical reorganization revealed by optical recording of cat primary visual cortex. Nature *375*, 780–784.

Das, A., and Gilbert, C.D. (1997). Distortions of visuotopic map match orientation singularities in primary visual cortex. Nature *387*, 594–598.

DeYoe, E.A., Carman, G.J., Bandettini, P., Glickman, S., Wieser, J., Cox, R., Miller, D., and Neitz, J. (1996). Mapping striate and extrastriate visual areas in human cerebral cortex. Proc. Natl. Acad. Sci. USA *93*, 2382–2386.

Dräger, U.C. (1975). Receprive field of single cells and topography in mouse visual cortex. J. Comp. Neurol. *160*, 269–290.

Engel, S.A., Rumelhart, D.E., Wandell, B.A., Lee, A.T., Glover, G.H., Chichilnisky, E.-J., and Shadlen, M.N. (1994). FMRI of human visual cortex. Nature *369*, 525.

Engel, S.A., Glover, G.H., and Wandell, B.A. (1997). Retinotopic organization in human visual cortex and the spatial precision of functional MRI. Cereb. Cortex *7*, 181–192.

Frostig, R.D., Lieke, E.E., Ts'o, D.Y., and Grinvald, A. (1990). Cortical functional architecture and local coupling between neuronal activity and the microcirculation revealed by in vivo high-resolution optical imaging of intrinsic signals. Proc. Natl. Acad. Sci. USA *87*, 6082–6086.

Gordon, J.A., and Stryker, M.P. (1996). Experience-dependent plasticity of binocular responses in the primary visual cortex of the mouse. J. Neurosci. *16*, 3274–3286.

Grinvald, A., Lieke, E., Frostig, R.D., Gilbert, C.D., and Wiesel, T.N. (1986). Functional architecture of cortex revealed by optical imagingof intrinsic signals. Nature *324*, 361–364.

Hubel, D.H., and Wiesel, T.N. (1974). Uniformity of monkey striate cortex: a parallel relationship between field size, scatter, and magnification factor. J. Comp. Neurol. *158*, 295–306.

Issa, N.P., Trepel, C., and Stryker, M.P. (2000). Spatial frequency maps in cat visual cortex. J. Neurosci. *20*, 8504–8514.

Malonek, D., and Grinvald, A. (1996). Interactions between electrical activity and ortical microcirculation revealed by imaging spectroscopy: implications for functional brain mapping. Science *272*, 551–554.

Mangini, N.J., and Pearlman, A.L. (1980). Laminar distribution of receptive field properties in the primary visual cortex of the mouse. J. Comp. Neurol. *193*, 203–222.

Margoliash, D. (1983). Acoustic parameters underlying the responses of song-specific neurons in the white-crowned sparrow. J. Neurosci. *3*, 1039–1057.

Maunsell, J.H., and Van Essen, D.C. (1983). Functional properties of neurons in middle temporal visual area of the macaque monkey. I. Selectivity for stimulus direction, speed, and orietation. J. Neurophysiol. *49*, 1127–1147.

Mayhew, J.E.W., Askew, S., Zheng, Y., Porrill, J., Westby, G.W.M., Redgrave, P., Rector, D.M., and Harper, R.M. (1996). Cerebral vasomotion: a 0.1-Hz oscillation in reflected light imaging of neural activity. Neuroimage *4*, 183–193.

Métin, C., Godement, P., and Imbert, M. (1988). The primary visual cortex in the mouse: receptive field properties and functional organization. Exp. Brain Res. *69*, 594–612.

Mitra, P.P., Pesaran, B., and Kleinfeld, D. (1999). Analysis of dynamic optical imaging data. In Imaging Neurons: A Laboratory Manual, R. Yuste, F. Lanni, and A. Konnerth, eds. (Cold Spring Harbor, NY: Cold Spring Harbor Laboratory Press), pp. 9.1–9.9.

Olavarria, J., and Montero, V.M. (1989). Organization of visual cortex in the mouse revealed by correlating callosal and striate-extrastriate connections. Vis. Neurosci. *3*, 59–69.

Olavarria, J., Mignano, L.R., and Van Sluyters, R.C. (1982). Pattern of extrastriate visual areas connecting reciprocally with striate cortex in the mouse. Exp. Neurol. *78*, 775–779.

Schuett, S., Bonhoeffer, T., and Hubener, M. (2002). Mapping retinotopic structure in mouse visual cortex with optical imaging. J. Neurosci. *22*, 6549–6559.

Sereno, M.I., Dale, A.M., Reppas, J.B., Kwong, K.K., Belliveau, J.W., Brady, T.J., Rosen, B.R., and Tootell, R.B.H. (1995). Borders of multiple visual areas in humans revealed by functional magnetic resonance imaging. Science *268*, 889–893.

Shoham, D., Glaser, D.E., Arieli, A., Kenet, T., Wijnbergen, C., Toledo, Y., Hildesheim, R., and Grinvald, A. (1999). Imaging cortical dynamics at high spatial and temporal resolution with novel blue voltage-sensitive dyes. Neuron *24*, 791–802.

Wagor, E., Mangini, N.J., and Pearlman, A.L. (1980). Retinotopic organization of striate and extrastriate visual cortex in the mouse. J. Comp. Neurol. *193*, 187–202.

White, L.E., Bosking, W.H., Williams, S.M., and Fitzpatrick, D. (1999). Maps of central visual space in ferret V1 and V2 lack matching inputs from the two eyes. J. Neurosci. *19*, 7089–7099.

Williams, R.W., Strom, R.C., Rice, D.S., and Goldowitz, D. (1996). Genetic and environmental control of variation in retinal ganglion cell number in mice. J. Neurosci. *16*, 7193–7205.

Zeki, S.M. (1974). Functional organization of a visual area in the posterior bank of the superior temporal sulcus of the rhesus monkey. J. Physiol. *236*, 549–573.

Zeki, S.M. (1980). The response properties of cells in the middle temporal area (area MT) of owl monkey visual cortex. Proc. R. Soc. London B Biol. Sci. *207*, 239–248.